Nuclear Instruments and Methods in Physics Research A 797 (2015) 234–246

Contents lists available at ScienceDirect

Nuclear Instruments and Methods in Physics Research A

journal homepage: www.elsevier.com/locate/nima

Time-resolved momentum and beam size diagnostics for bunch trains with very large momentum spread

M. Olvegård [a], M.J. Barnes [b], L. Ducimetière [b], V. Ziemann [a]

[a] Uppsala University, Department of Physics and Astronomy, Box 516, 751 20 Uppsala, Sweden
[b] CERN, European Organization of Nuclear Research, 1211 Genève 23, Switzerland

ARTICLE INFO

Article history:
Received 10 February 2015
Received in revised form
24 June 2015
Accepted 28 June 2015
Available online 10 July 2015

Keywords:
Beam size measurement
Energy measurement
Spectrometry
CLIC
Electron decelerator
Time-resolved diagnostics

ABSTRACT

We propose a novel method to measure the time-resolved momentum distribution and size of beams with very large momentum spread. To demonstrate the principle we apply the method to the beam at the end of a Compact Linear Collider decelerator, where conventional diagnostic methods are hampered by the large energy spread of the drive beam after up to 90% of its kinetic energy is converted into microwave power. Our method is based on sweeping the beam in a circular pattern to determine the momentum distribution and recording the beam size on a screen using optical transition radiation. We present an algorithm to extract the time-resolved momentum distribution. Furthermore, the beam size along the bunch train can be extracted from the image left on a screen by sweeping the beam linearly. We introduce the analysis technique and show simulation results that allow us to estimate the applicability. In addition, we present a conceptual design of the technical realization.

1. Introduction

We discuss a method to determine the time-resolved momentum spread and beam size of bunch-trains with very large momentum spread by using time-varying transversely deflecting fields. This work was stimulated by the very large momentum spread occurring in the decelerator of the Compact Linear Collider [1].

Before delving into the analysis, we note that our methodology is related to the widely used method of using time-varying transverse fields to obtain information about the beam, first mentioned in Ref. [2] and experiments reported in [3]. In the early works the emphasis was on separating particles with different masses, later it was realized that fast-varying fields can be used to measure properties of bunches, too short to be analyzed using other methods, such as streak cameras. First results using circular deflectors for bunch length diagnostics appeared soon thereafter [4], and is still used to diagnose short bunches [5,6]. With the advent of free-electron lasers (FEL) and the need for ultra-short bunches with moderate momentum spread the radio-frequency deflectors experienced a renaissance, reported in the late 1990s [7]. Today, beam diagnostics using transversely deflecting structures is commonly used to measure the momentum spread and the transverse emittance of an ultra-short bunch as a function of the longitudinal position [8–11], the so-called slice momentum spread, and slice emittance, as important parameters for successful operation of FELs. The challenges of diagnosing beams with large momentum spread have been studied regarding emittance measurements [12,13] as well as for momentum diagnostics [14].

The present work is inspired by the development of using deflecting fields to measure time-dependent properties of the beam, but instead of focusing on the ultra-short time-scale needed for single-bunch diagnostics, we focus on the difficulties to diagnose the very large momentum spread that appears naturally as novel acceleration schemes are explored, e.g. in CLIC. The beams in CLIC after the interaction point have large momentum spread due to large losses from the emission of beamstrahlung in the collisions. This spread could be monitored as a complementary diagnostic, for the luminosity, to other methods discussed in [15]. A second subsystem of CLIC where extremely large momentum spread is encountered is the drive beam decelerator, where up to 90% of the incoming beam power is extracted from the drive beam [1,16]. The situation where the beams are constant or averaged in time was already investigated in [14,17], but in this report we extend the analysis to accelerators that are pulsed and momentum spread varies along the pulse train. This is an important quantity to measure, because it is a measure of the quality of the interaction, either the luminosity, or the power extraction in the CLIC decelerator. The latter is the system on which we base the discussion in the remainder of this report.

In CLIC the deceleration leaves the beam with the energy distribution depicted in Fig. 1, with a high energy transient at

E-mail address: maja.olvegard@physics.uu.se (M. Olvegård).

http://dx.doi.org/10.1016/j.nima.2015.06.063
0168-9002/

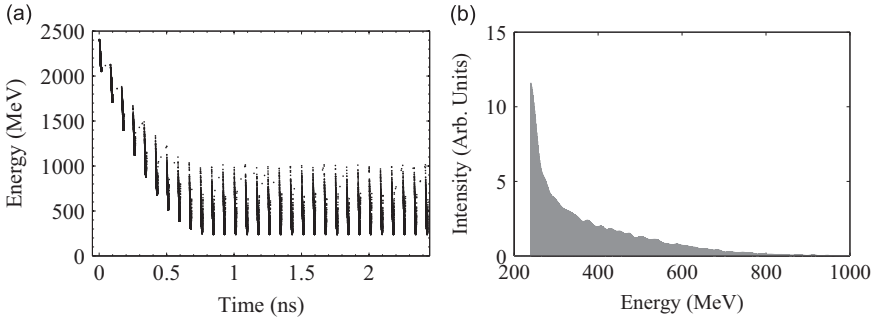

Fig. 1. The energy distribution in the decelerated CLIC drive beam, simulated with PLACET [18]. The high energy transient (a) extends all the way up to the initial energy of 2.4 GeV and is followed by a 240 ns long steady-state. The transient contains very few particles compared to the rest of the bunch train and the histogram to the right (b) shows the energy content of the steady-state only (a) Energy transient, (b) Histogram of the steadystate.

the head of the bunch train, shown in Fig. 1(a), reaching all the way to the initial energy. The majority of the bunches, in the steady state of the pulse, lose 90% of their energy. The resulting energy distribution, shown in Fig. 1(b) has a peak around the minimum energy with a long tail extending to higher energies. The stability of the drive beam under deceleration was identified as a crucial issue among others for the feasibility of CLIC [19]. This motivated the construction of the CLIC Test Facility (CTF3) [20] to experimentally address the issue, in particular how the momentum distribution in the beam can be monitored for an optimum setup of the decelerator.

In the test beam line (TBL) of CTF3, the drive beam decelerator is experimentally studied in small-scale [21]. The analysis of the beam profile diagnostics in TBL in Refs. [22,23] has shown that segmented beam dumps, though currently used for time-resolved spectrometry in TBL, are not suitable for the CLIC decelerators due to the high beam power. On the other hand, OTR screens have a good chance of sustaining the high intensity, assuming that it is sufficiently diluted. We therefore intend to base the time-resolved measurements of transverse and energy profile on OTR screens.

The general layout envisioned for the diagnostics is to have two scanning kicker magnets sitting close together in the beam line; one kicking in the vertical direction and the other in the horizontal direction, similar to the dilution kickers in the LHC dump line, which forms the figure "e" of the beam on a screen [24,25]. We assume that the kickers are excited in a cycle corresponding to the 240 ns drive beam duration and with a rise of the magnetic field that provides a kick from zero to a few milliradian in the same time range. Furthermore, we assume that the magnets are excited such that the horizontal kicker is driven by a cosine wave while the vertical is driven by a sine wave, thus creating a Lissajous figure of the beam on the screen. Forming the sweep into a circle allows us to analyze the momentum distribution along the beam pulse. A linear sweep in one direction at a time gives information about the transverse beam distribution along the pulse. The deflection cycle of a few hundred nanoseconds means that we focus on diagnosing variations along a bunch train rather than on single-bunch diagnostics, and, that the steady-state is favored over the transient.

We will begin with discussing spectrometry for large momentum spread beams and then turn to the particular measurement setup proposed. There, we will first predict what will be seen on the screen for a given beam distribution in time and momentum when the circular sweep is applied. Secondly, we will show examples of the measurement and of the analysis. Then, we discuss the time-resolved beam size measurement. Lastly, we present a conceptual design of the fast kicker magnet system together with a thermal–mechanical study of potential screen materials, with the particular case of the CLIC decelerator in mind.

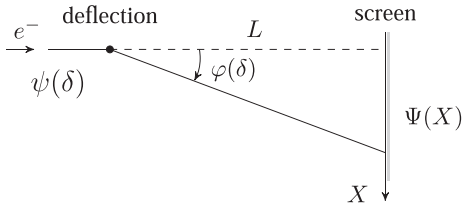

Fig. 2. Sketch of a horizontal deflection onto a screen, defining the variables used in the equations.

2. Spectrometry for beams with large momentum spread

In a spectrometer the beam is deflected by a dipole magnet with field B and length l. Since the deflection angle $\varphi = Bl/pc$ depends inversely on the momentum p of the beam particles, particles with different momenta after a distance L from the center of the dipole intercept a downstream screen at different positions $X = L\tan\varphi$. See Fig. 2 for an illustration of the geometry. Since we anticipate very large momentum spread we restrict ourselves to small deflection angles φ such that we can use the approximation $\tan\varphi \approx \varphi$. Parametrizing the momentum by $\delta = (p - p_0)/p_0$ where p_0 is the reference momentum of the beam and φ_0 the deflection angle for the reference beam, we can write

$$X = \frac{D_0}{1+\delta} \tag{1}$$

where we introduce the abbreviation $D_0 = L\varphi_0$. Incidentally, D_0 coincides with the dispersion generated by the dipole. If the momentum spread is small, i.e. when $\delta \ll 1$, we obtain the linear approximation $X \approx D_0(1-\delta)$. In our case, however, this assumption is not valid. Instead, we use Eq. (1) to determine the particle density on the screen by integrating over all initial momenta through

$$\Psi(X) = \int \psi(\delta)\, \delta_D\left(X - \frac{D_0}{1+\delta}\right) d\delta \tag{2}$$

where δ_D denotes the Dirac delta function. The interpretation of the previous equation is straightforward: We start with a momentum distribution $\psi(\delta)$ of the beam and the delta function collects all the δ that end up at a particular position X on the screen. For the integration over δ we use the relation

$$\delta_D(h(u)) = \sum_i \frac{\delta_D(u-u_i)}{|h'(u_i)|} \quad \Longrightarrow \int f(u)\delta_D(h(u))du = \sum_i \frac{f(u_i)}{|h'(u_i)|} \tag{3}$$

where u_i are the zeros of $h(u)$. In our case, $h(\delta) = X - D_0/(1+\delta)$ with one zero at $\delta = (D_0 - X)/X$ and with $h'(\delta_0) = X^2/D_0$. The

particle distribution on the screen is then given by

$$\Psi(X) = \frac{D_0}{X^2}\psi\left(\frac{D_0 - X}{X}\right) \tag{4}$$

where X is the coordinate on the screen in the plane of deflection and D_0 is the reference dispersion, e.g. for the position of the momentum peak.

Normally, we are interested in deducing the moment profile from the geometric profile on a spectrometer screen. To do so we need the inverse transformation. It is calculated in the same way and reads

$$\psi(\delta) = \int \Psi(X)\delta_D\left(\delta - \frac{D_0 - X}{X}\right) dX = \frac{D_0}{(1+\delta)^2}\Psi\left(\frac{D_0}{1+\delta}\right). \tag{5}$$

If, instead of using Eq. (5) to analyze such a spectrometer distribution, we use the linear approximation $X \approx D_0(1-\delta)$ we commit an error. The magnitude of this error is demonstrated in Fig. 3, where we have assumed a Gaussian momentum distribution with rms spread Δ_0 and peak momentum p_0. The momentum distribution extracted from a spectrometer measurement using the linear dispersion function will appear to have a higher peak momentum p_p than the true value p_0. At the same time, the extracted spread Δ is an underestimation of the real momentum spread, an effect that grows as Δ_0 grows.

The resolution of the presented method can be estimated from solving Eq. (1) by calculating the derivative with respect to X. This yields the amplification factor $d\delta/dX = -D_0/X^2$ by how much a small uncertainty in position on the screen X affects the relative momentum δ. If the transverse rms beam size of the undeflected beam is σ_x, the rms resolution of the relative momentum σ_δ is given by

$$\sigma_\delta = \frac{D\sigma_x}{X^2}. \tag{6}$$

We note that the resolution for δ is not constant, but depends on the position on the screen X and diverges near the axis for $X = 0$ where all the high energy particles are positioned. The best resolution we find for the low-momentum particles that are deflected the most. For particles at the reference energy $\delta = 0$ and $X = D_0$ from Eq. (1) we find the expected result that $\sigma_\delta = \sigma_x/D_0$.

Now that we have established the correct way of analyzing spectrometer profiles for large momentum spreads we turn to discuss a method to obtain time-resolved information about the beam pulse.

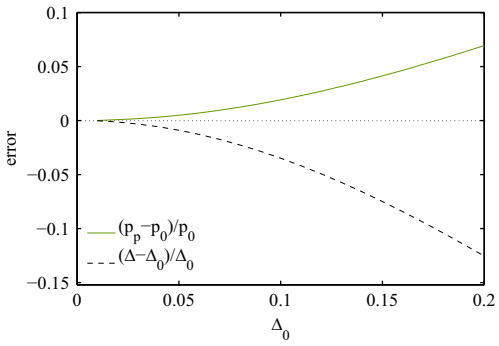

Fig. 3. The error on extracted peak momentum p_p and spread Δ when using linear dispersion to analyze a spectrometer measurement on beams with Gaussian momentum distribution with peak momentum p_0 and rms spread Δ_0.

3. Time-resolved spectrometry

In order to extract time-resolved information from the spectrometer measurement we first look at how a particle distribution transforms when projected onto a screen. We use the variables defined in Fig. 2 and introduce a rotating effective magnetic field vector so that a particle with momentum δ hits the screen at the coordinates

$$X = \frac{L\varphi_0\cos(2\pi\tau)}{1+\delta}, \quad Y = \frac{L\varphi_0\sin(2\pi\tau)}{1+\delta} \tag{7}$$

with $\tau = t/T$ where T is the period of the magnetic cycle and $0 < \tau < 1$. Note that the magnet sprays the beam on a sector of a circle on the screen. The cycle time T has to be matched to the bunch train duration in order to avoid overlap of the tail with the head of the beam.

Let further $\psi(\tau,\delta)$ be the initial particle density distributed over time and momentum. We neglect for now the emittance and obtain the transverse particle distribution on the screen $\Psi(X,Y)$ by integrating over time and momentum through

$$\Psi(X,Y) = \int \psi(\tau,\delta)\delta_D\left(X - \frac{L\varphi_0\cos(2\pi\tau)}{1+\delta}\right) \times\delta_D\left(Y - \frac{L\varphi_0\sin(2\pi\tau)}{1+\delta}\right) d\tau\, d\delta. \tag{8}$$

This is an integral over two dimensions and we use the Jacobi determinant to transform the integration variables from (τ,δ) to (X,Y). It is defined through

$$\det(J) = \begin{vmatrix} \partial X/\partial\tau & \partial X/\partial\delta \\ \partial Y/\partial\tau & \partial Y/\partial\delta \end{vmatrix}. \tag{9}$$

With the Jacobi determinant the integral in Eq. (8) transforms as

$$\Psi(X,Y) = \int \psi(\tau,\delta)\delta_D\left(\tau - \frac{1}{2\pi}\arctan\left(\frac{Y}{X}\right)\right) \times\delta_D\left(\delta + 1 - \frac{l\varphi_0}{\sqrt{X^2+Y^2}}\right)\frac{1}{|\det(J)|}\, d\tau\, d\delta \tag{10}$$

where we use the fact that

$$X^2 + Y^2 = \left(\frac{L\varphi_0}{1+\delta}\right)^2 \quad \text{and} \quad \frac{Y}{X} = \tan(2\pi\tau). \tag{11}$$

The matrix elements for the determinant are easily derived through differentiation with the result

$$\frac{\partial X}{\partial\tau} = -2\pi\frac{L\varphi_0}{1+\delta}\sin(2\pi\tau) = -2\pi Y$$
$$\frac{\partial X}{\partial\delta} = -\frac{L\varphi_0}{(1+\delta)^2}\cos(2\pi\tau) = -\frac{X}{1+\delta}$$
$$\frac{\partial Y}{\partial\tau} = 2\pi\frac{L\varphi_0}{1+\delta}\cos(2\pi t) = 2\pi X$$
$$\frac{\partial Y}{\partial\delta} = -\frac{L\varphi_0}{(1+\delta)^2}\sin(2\pi t) = -\frac{Y}{1+\delta}$$

with the resulting determinant

$$\det(J) = \frac{2\pi}{1+\delta}\left(X^2+Y^2\right) = \frac{2\pi}{L\varphi_0}\left(X^2+Y^2\right)^{3/2}. \tag{12}$$

Finally, we express the distribution on the screen purely in the spatial variables X and Y:

$$\Psi(X,Y) = \frac{L\varphi_0}{2\pi}\frac{1}{(X^2+Y^2)^{3/2}} \times \psi\left(\frac{1}{2\pi}\arctan\left(\frac{Y}{X}\right), \frac{L\varphi_0}{\sqrt{X^2+Y^2}} - 1\right). \tag{13}$$

This equation relates the momentum distribution $\psi(\tau,\delta)$, which originally was a function of the momentum δ and time τ along the

pulse, to coordinates on the screen and therefore describes how the image on the screen is related to a given time dependent momentum distribution along the pulse.

We now turn to extracting the original time dependent momentum distribution ψ from an image on the screen produced by the rotating magnetic field. For this we need to invert the procedure discussed in the previous section and determine the original time-dependent momentum distribution $\psi(\tau,\delta)$ from the distribution on the image $\Psi(X,Y)$. The inverse procedure starts similarly with a two-dimensional integral:

$$\psi(\tau,\delta) = \int \Psi(X,Y)\delta_D\left(\tau - \frac{1}{2\pi}\arctan\left(\frac{Y}{X}\right)\right) \times\delta_D\left(\delta+1-\frac{L\varphi_0}{\sqrt{X^2+Y^2}}\right) dX\,dY. \tag{14}$$

We now need the Jacobian for the inverse system $\tilde{J}$, for which the elements are as follows:

$$\begin{aligned}\frac{\partial\tau}{\partial X} &= -\frac{1}{2\pi}\frac{Y}{X^2+Y^2}\\ \frac{\partial\tau}{\partial Y} &= \frac{1}{2\pi}\frac{X}{X^2+Y^2}\\ \frac{\partial\delta}{\partial X} &= -L\varphi_0\frac{X}{(X^2+Y^2)^{3/2}}\\ \frac{\partial\delta}{\partial Y} &= -L\varphi_0\frac{Y}{(X^2+Y^2)^{3/2}}.\end{aligned} \tag{15}$$

With this Jacobian $\tilde{J}$, which is the inverse of J used in Eq. (12), and its determinant

$$\det(\tilde{J}) = \frac{L\varphi_0}{2\pi}\frac{1}{(X^2+Y^2)^{3/2}} = \frac{(1+\delta)^3}{2\pi(L\varphi_0)^2} \tag{16}$$

we have inverted the procedure and can analyze a measurement of the screen profile through

$$\psi(\tau,\delta) = \frac{2\pi(L\varphi_0)^2}{(1+\delta)^3}\Psi\left(\frac{L\varphi_0\cos(2\pi\tau)}{1+\delta}, \frac{L\varphi_0\sin(2\pi\tau)}{1+\delta}\right). \tag{17}$$

The momentum information is now encoded in the radial variable on the screen and the temporal information is in the angle, in accordance with Eq. (11).

In order to determine the resolution of the method we assume that the distributions in time, momentum and transverse size due to emittance are Gaussian and constant along the bunch train. Under these assumptions we determine the scaled arrival time σ_τ and the relative momentum spread σ_δ. Note, that in the general case, even a correlation $\sigma_{\tau\delta}$ between τ and δ can appear. These parameters constitute the covariance matrix and we can calculate it using conventional error propagation techniques, using the Jacobian $\tilde{J}$ given in Eq. (15):

$$\begin{pmatrix}\sigma_\tau^2 & \sigma_{\tau\delta}\\ \sigma_{\tau\delta} & \sigma_\delta^2\end{pmatrix} = \tilde{J}\begin{pmatrix}\sigma_x^2 & \sigma_{xy}\\ \sigma_{xy} & \sigma_y^2\end{pmatrix}\tilde{J}^T \tag{18}$$

where $\tilde{J}^T$ denotes the transpose of the Jacobian $\tilde{J}$. The matrix containing σ_x, σ_y and a possible correlation term σ_{xy} due to coupling is the projection of the beam matrix onto the screen. If we now simplify the calculation by assuming an uncoupled, and round beam with rms size $\sigma_x=\sigma_y=\sigma_r$ a straightforward evaluation of the previous equation yields

$$\sigma_\tau = \frac{\sigma_r}{2\pi R} \quad\text{and}\quad \sigma_\delta = \frac{L\varphi_0\sigma_r}{R^2} \tag{19}$$

with the abbreviation $R^2 = X^2+Y^2 = (L\varphi_0/(1+\delta))^2$. This result is also intuitively appealing. The rms beam size, σ_r, divided by the circumference at a given radius gives the resolution for the scaled time τ and the result for the momentum δ is the same as for the one-dimensional case already discussed in Section 2. In practice, the resolution is ultimately set by the resolution of the screen image, i.e. the camera pixel size.

For the evaluation of the performance we have chosen a particle distribution whose momentum along the pulse varies sinusoidally with amplitude $\delta=0.1$. The assumed rms momentum spread δ has the same magnitude. This momentum distribution, shown in Fig. 4(a), results in the image on the screen shown in Fig. 4(b). The geometric beam size on the screen is assumed to be small compared to the beam size due to the large momentum spread. In the simulation we assume a deflection angle $\varphi_0=1$ mrad and drift length $L=5$ m. Using the procedure outlined above, to extract the momentum distribution from the image, indeed results in a distribution that is indistinguishable from the one shown in Fig. 4(a). In the numerical simulations described here we have employed Delaunay triangulation [26] for the nonlinear transformation from the Cartesian coordinates (X,Y) to the polar coordinates (δ,τ).

In order to investigate the robustness of the inversion we add random noise to the image in Fig. 4(b). The maximum noise is set to 10% of the maximum intensity in the original image and the noise is uniform in shape and centered around zero. Fig. 5 (b) shows the image with noise. Before extracting the momentum distribution we select the region of interest on the screen and set the pixel values on the edges to zero. This is a precaution for avoiding a strong enhancement of the noise close to the singularity as $\delta\to-1$. The singularity can be discarded since it corresponds to particles at rest. Then, by extracting the distribution we obtain Fig. 5(a). The shape and position of the snake figure remains intact, although the noise perturbs the visual impression of the distribution, especially in the low-momentum region. This occurs because

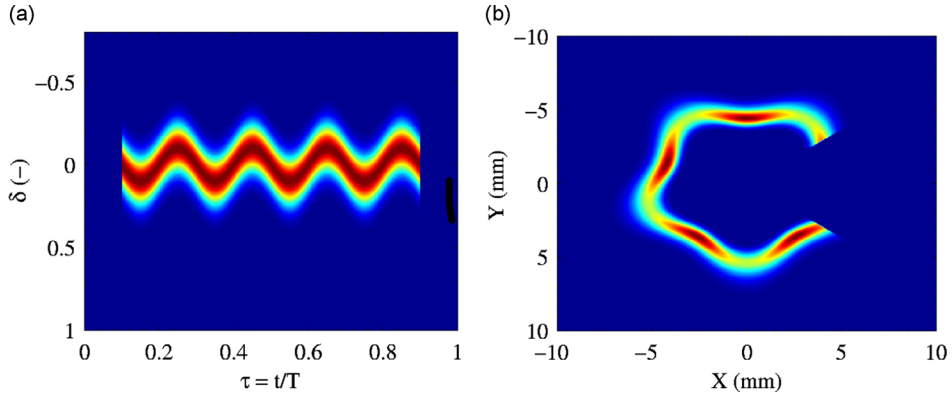

Fig. 4. Reference distribution (a) and screen image (b). The momentum spread is 10% along the pulse while the average momentum oscillates with an amplitude equal to the 1σ spread.

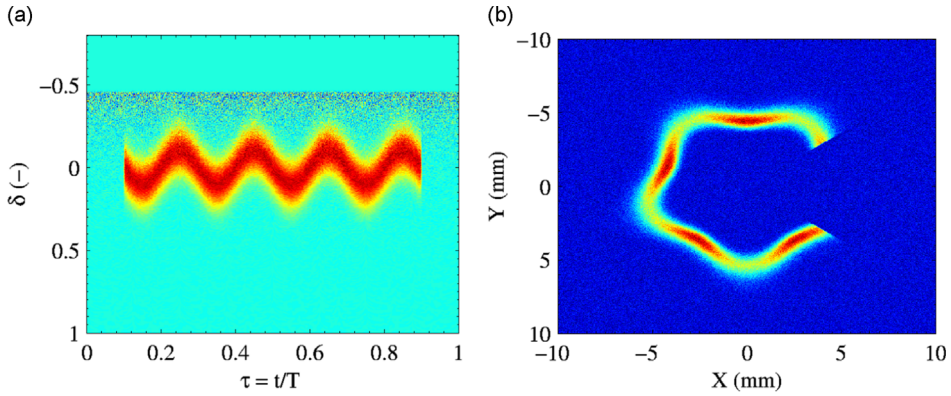

Fig. 5. Screen image (b) and corresponding extracted momentum distribution (a) where noise has been added. The noise is uniformly distributed around zero, with a maximum amplitude of 10% of the maximum intensity in the original image. Before inverting the image we set the pixels on the edges of the screen to zero in order to avoid a blow up near the singularity as δ approaches -1.

the transformation between the momentum distribution and the image in Eq. (13) is nonlinear and the low-momentum part is enhanced due to the denominator $(1+\delta)^3$ in Eq. (17).

A finite emittance will smooth out the profile on the screen, but if the geometric beam size is small compared to the dispersive beam size $\sigma_0 = L\varphi_0\Delta$ on the screen, the system can still be inverted and the initial distribution regained by applying Eq. (17). In Fig. 6 we demonstrate the effect of a finite emittance by calculating the convolution of the original screen image from Fig. 4 with the geometric beam profile. The column to the right shows the screen images and the left column the corresponding distribution extracted from each image without taking the finite emittance into account. The geometric beam size $\sigma_{x,y}$ in the rows is given by 0.2, 1, and 2 in units of the beam width due to the momentum spread σ_0. We note that qualitative information can be extracted from the screen even for very large emittances. The general trend is that the extracted momentum spread increases with increasing emittance, while the extracted average momentum decreases.

Our goal is to perform these measurements on the decelerated CLIC drive beam, and therefore we show it in Fig. 7. The original momentum distribution shown in Fig. 7(a) is taken from Fig. 1(b), where we have let the momentum profile be constant along the bunch train. By applying Eq. (13) we obtain the corresponding screen image in Fig. 7(b), which can be brought back to the original distribution through Eq. (17).

To the image in Fig. 7(b) we now add random noise which is uniformly distributed around zero with an amplitude of 10% of the maximum intensity in the original image. Fig. 8 shows the new image with noise. As in the previous example of noise handling in Fig. 5 we ignore the contribution from the edges before we extract the momentum distribution. The result presented in Fig. 8(a) has the same features as the original distribution and we conclude that the extraction algorithm is rather insensitive to noise.

In the CLIC decelerator the finite emittance is not expected to influence the measurement notably. Although the emittance is fairly large (150 mm mrad), the momentum spread is so large that even with a very small dispersion the geometric beam size will be negligible in comparison. In the next section we will discuss the beam size measurements, which can also be used for emittance measurements.

4. Time-resolved beam size measurements

For time-resolved beam size measurements in one plane, say horizontal, we make a linear sweep in the other, here vertical, direction. Variations in the horizontal beam size along the pulse will then show up as variations of the horizontal width of the image on the screen, where time along the pulse is encoded in the vertical position. One horizontal slice of the image thus corresponds to the horizontal profile of a given temporal slice in the pulse. A large momentum spread, however, will cause vertical smearing of particles from one temporal slice across neighboring temporal slices. In this way the large momentum spread entangles the momentum and beam size distributions. Note that this smearing is more complex than plain convolution, because the degree of smearing depends on the deflection angle and therefore varies along the pulse.

We consider once more a beam with momentum distribution ψ. For simplicity, we let it be constant along the bunch train, although the same algorithm can be generalized to distributions that vary in time. For a bunch with arrival time τ_j the vertical position of an on-momentum particle is given by $D_0(\tau_j) = \alpha\tau_j$, where α is the linear sweep speed. As before, the particle density on the screen is calculated using Eq. (4) but this time the reference position is time-dependent. If we look at a slice of width dY at position $Y_k = \alpha\tau_k$ on the screen we can express the particle density in this slice k from the bunch arriving at τ_j as

$$\Psi(Y_k) = \frac{D_0(\tau_j)}{Y_k^2}\psi\left(\frac{D_0(\tau_j)-Y_k}{Y_k}\right) = \frac{\tau_j}{\alpha\tau_k^2}\psi\left(\frac{\tau_j-\tau_k}{\tau_k}\right). \tag{20}$$

We assume that the momentum distribution is normalized to unity and calculate the fraction f_{kj} of particles in a temporal slice of width $d\tau = dY/\alpha$ that overlaps with another to

$$f_{kj} = \Psi(Y_k)dY = \frac{\tau_j}{\alpha\tau_k^2}\psi\left(\frac{\tau_j-\tau_k}{\tau_k}\right)\alpha\, d\tau = \frac{\tau_j d\tau}{\tau_k^2}\psi\left(\frac{\tau_j-\tau_k}{\tau_k}\right). \tag{21}$$

The fact that α disappears from the expression is predominantly a consequence of choosing scaled variables, here the time τ, and considering the fraction of the particles.

Now, we consider a geometric particle density $g_j(X)$ that may vary from one time-slice j to another. The total density distribution in slice k of the screen is calculated as the sum of contributions from all bunches $j = 1, \ldots, n$ through

$$r_k(X) = \sum_{j=1}^{n} f_{kj} g_j(X). \tag{22}$$

The same equation holds for every horizontal position X. The indices k and j label different time slices and, in particular, f_{kj} represents how much time-slice j leaks into the slice k, that only were to contain the particles from time-slice k, were the beam mono-chromatic. With this formulation the momentum smearing during the linear sweep is turned into the matrix equation:

$$R = FG \tag{23}$$

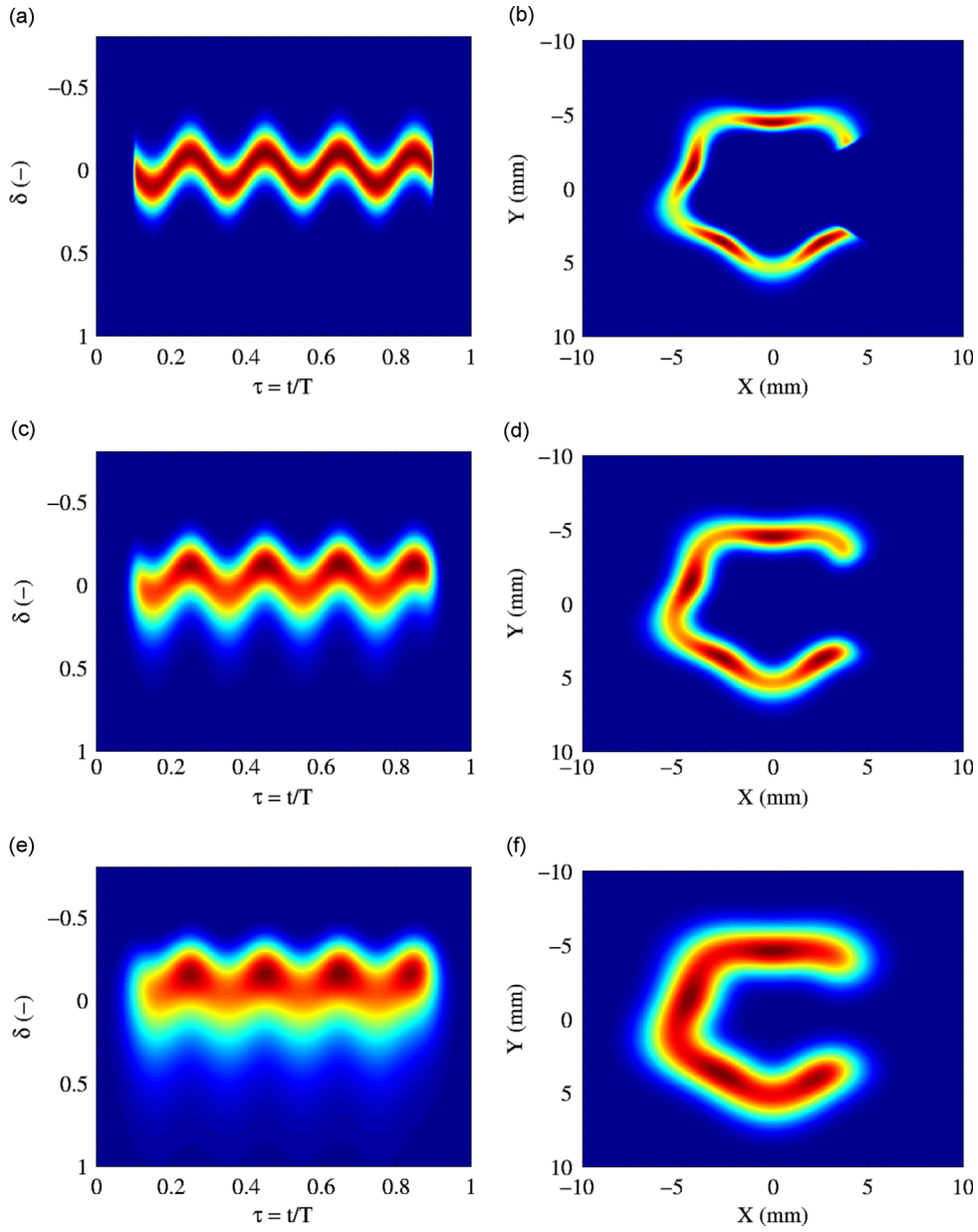

Fig. 6. The extracted momentum distribution (left column) corresponding to each screen image (right column) where for every row the geometric beam size $\sigma_{x,y}$ increases compared to the dispersive beam size $\sigma_0 = L\varphi_0\Delta$. Note that the first bunch, corresponding to $\tau = 0.1$, is imaged in the lower right corner of the image in the column to the right. (a) Extracted distribution and (b) screen image for $\sigma_{x,y}/\sigma_0 = 0.2$, (c) Extracted distribution and (d) screen image for $\sigma_{x,y}/\sigma_0 = 1$, (e) Extracted distribution and (f) screen image for $\sigma_{x,y}/\sigma_0 = 2$.

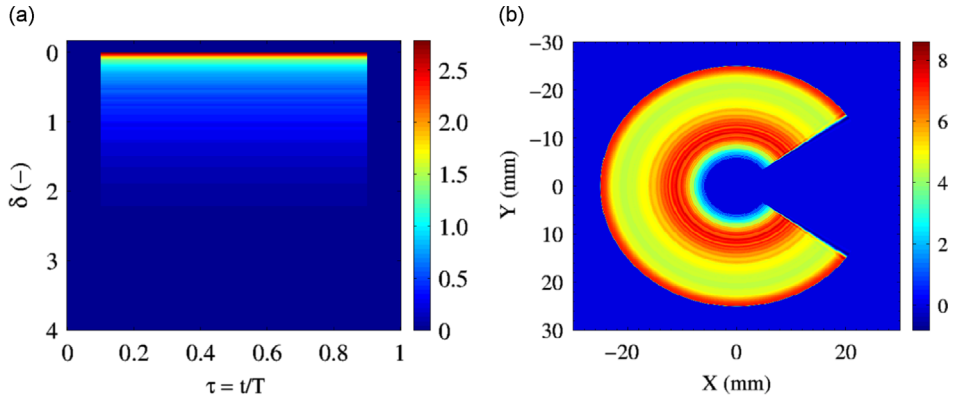

Fig. 7. The CLIC momentum distribution (a) transformed to an image in the post-PETS diagnostic line (b). We have used $L = 5$ m and $\varphi_0 = 5$ mrad. The head of the pulse, corresponding to the time $\tau = 0.1$, is in the lower right corner of the screen image (b).

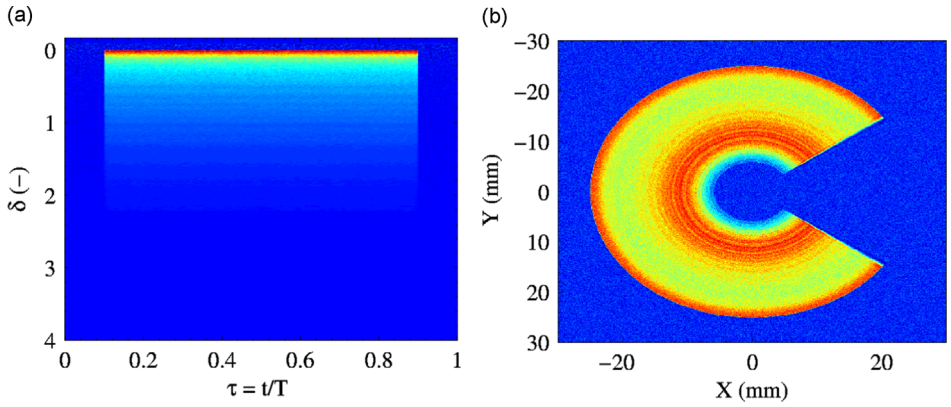

Fig. 8. The CLIC momentum distribution (a) extracted from an image with 10% noise (b).

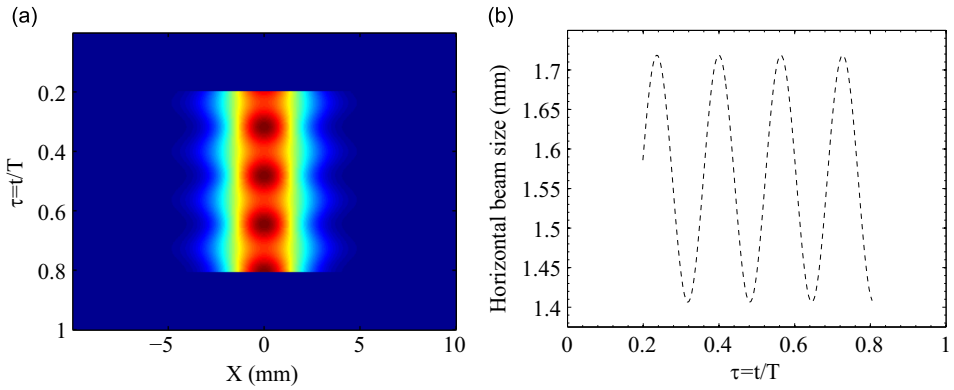

Fig. 9. The geometric distribution varies with time in the horizontal plane (a) with the rms beam size as shown in (b). The head of the bunch train is at $\tau = 0.2$ and the tail at $\tau = 0.8$. Large momentum spread distorts the distribution and the beam size measurement.

where R is the measured distribution, G is the corresponding distribution of a monochromatic beam and F contains the contamination function of the large momentum spread. For a monochromatic beam F is the identity matrix, meaning no cross-contamination of slices and a linear relation between distribution in time and distribution in the vertical plane. By computing $G = F^{-1}R$ the measured distribution is transformed to such a form that it is easily translated to the geometric distribution along the bunch train.

Assuming that the momentum distribution is known, e.g. through the measurement procedure described earlier, F can be calculated. The deconvolution problem is then reduced to the difficulty in finding the inverse F^{-1}. It may well be that F is numerically singular, such that F^{-1} strongly amplifies seemingly small densities, like noise, in the screen image R. One way of avoiding such singularities is through singular value decomposition (SVD) [27]: First reformulate $F^{-1} = (F^T F)^{-1} F^T$, where F^T is the transpose of F. Then, let $A = F^T F$ and apply SVD to the matrix A, which results in

$$A = U \Lambda U^T. \tag{24}$$

The matrix U is orthogonal with $U^{-1} = U^T$, and Λ is a diagonal matrix with diagonal elements λ_i. In this case, since F is symmetric, applying SVD is equivalent to calculating the matrix eigenvalues. Once these eigenvalues λ_i are known the computation of A^{-1} is trivial. However, if λ_i is zero or numerically close to zero Λ^{-1} will contain very large elements $1/\lambda_i$ that will amplify noise in the screen image. This can be avoided by forcing a cut-off value λ_{cut} such that if $\lambda_i < \lambda_{cut}$ let $1/\lambda_i = 0$. This procedure efficiently removes the subspace where the matrix F is degenerate. The cut-off value has to be chosen judiciously so that noise is suppressed while retaining the smearing information carried by λ_i. Alas, no general rule for the optimal cut-off can be given since it depends on the properties of the input distribution $g_j(X)$, the momentum distribution $\psi(\tau, \delta)$, as well as on the nature of the noise.

We investigate the reliability of the beam size measurement with a few examples. To this end we use a Gaussian particle distribution in the horizontal direction and introduce a modulation of the horizontal beam width along the bunch train as illustrated in Fig. 9. We first use a Gaussian momentum distribution of rms width Δ and we assume that the vertical beam size is negligible compared to the Gaussian momentum distribution. The vertical smearing of the horizontal distribution of a given temporal slice is thus only due to spreading of the momentum distribution, transformed to the image plane according to Eq. (4). As the momentum spread Δ grows, the beam size oscillations are damped until almost no variations are visible.

Fig. 10(a) shows the image of a beam with $\Delta = 0.1$ and Fig. 10 (b) contains the horizontal beam size extracted along the vertical direction as a solid line, together with the reference beam size taken from Fig. 9(b) shown as the dashed line. The large momentum spread hides the temporal beam size variation that would appear for a monochromatic beam. Using SVD with a carefully selected cut-off on the eigenvalue we retrieve the distribution in Fig. 11(a), very close to the input distribution from Fig. 9, and with a similar beam size variation displayed in Fig. 11(b).

Now we add noise to the original image in Fig. 10(a) before we apply the deconvolution algorithm. The noise is uniformly distributed around zero and we study how the analysis procedure handles different noise amplitudes. Fig. 12 shows the reconstructed distribution when the noise amplitude is 1% of the maximum intensity in the original image. Even though the

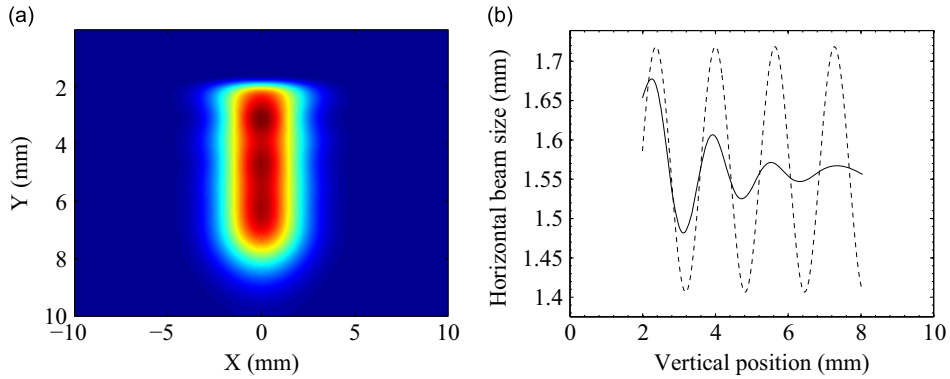

Fig. 10. Image of a beam where the momentum spread of $\Delta = 0.1$ hides the variation in horizontal beam width along the pulse (a). The rms horizontal beam width along the vertical direction extracted from the image is represented by the solid line in (b) together with the equivalent for a monochromatic beam from Fig. 9(b) as a dashed line. The first bunch is centered at approximately $Y = 2$ mm and the last bunch at $Y = 8$ mm.

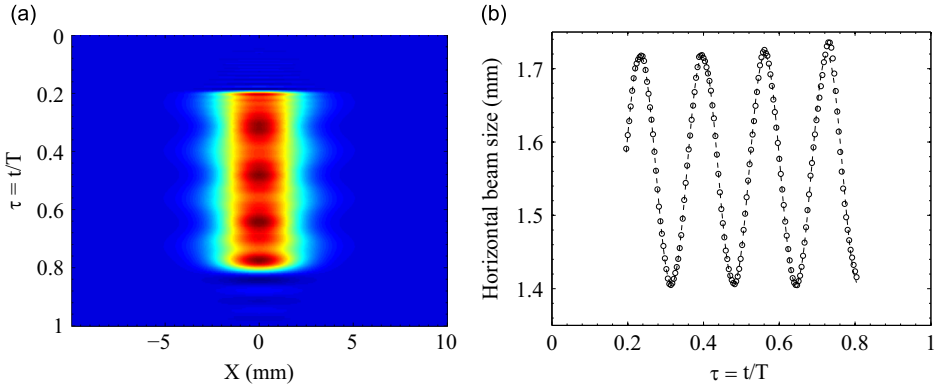

Fig. 11. The screen image in Fig. 10(a) deconvoluted using the SVD technique (a). The strong damping of the beam size variation is lifted and the extracted beam size follows the input variation (b) shown separately in Fig. 9.

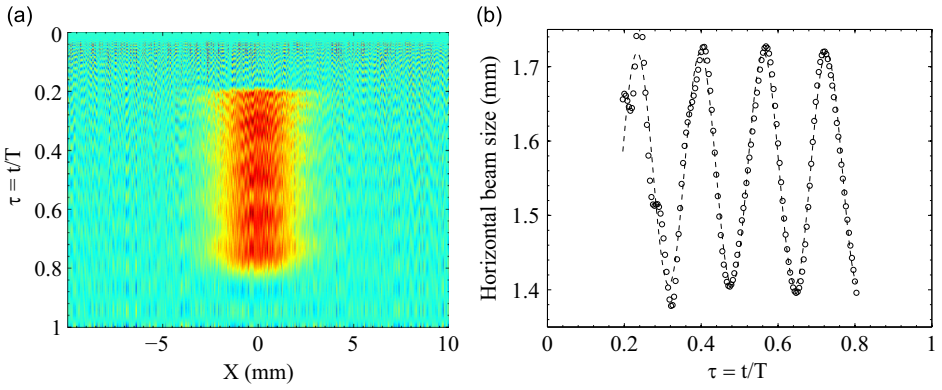

Fig. 12. Uniform noise with amplitude 1% of the maximum intensity has been added to the original image in Fig. 10(a). Then, through the matrix formulation in Eq. (23), the geometric distribution can be recovered (a). The extracted rms horizontal beam width along the pulse (b) agrees with the original input.

distribution is distorted by the noise, the extracted horizontal beam size in Fig. 12 is in agreement with the reference beam size from Fig. 9(b) displayed as the dashed line.

We now turn to a beam with CLIC parameters. Using only the steady-state part of the energy distribution from the histogram in Fig. 1(b) means that $0 < \delta < 4$. As before, we apply a linear sweep in the vertical direction and illustrate in Fig. 13 how the momentum profile is extended in the vertical direction of the screen for different points in time during the sweep. The later bunches are superimposed with the early bunches, which highlights the difficulty of extracting quantitative time information directly from the image.

Turning to the two-dimensional image, we use the geometric distribution in time from Fig. 9. Again, we apply a linear sweep in the vertical direction and obtain the screen image in Fig. 14(a). The horizontal beam size variation along the vertical axis is now hidden behind the momentum smearing. However, if we analyze the image slice by slice, moving in the vertical direction, a slight variation in beam size reveals itself, as seen as the solid line in Fig. 14(b). Though, this variation is distorted from the actual beam size, displayed in the same figure as the dashed line.

In order to recover the geometric density distribution along the bunch train we use the known momentum distribution to first compute the contamination matrix F. Subsequently, we solve the

matrix equation (23) and extract the corresponding monochromatic distribution G, which can easily be transformed to a temporal distribution, indistinguishable from the original distribution.

We repeat the experiment and add 1% random noise to the screen image in Fig. 14(a). Then, we apply the deconvolution algorithm to the noisy image and obtain the result displayed in Fig. 15. The extracted horizontal beam size in Fig. 15(b) still matches the reference beam size variation and we note that the reconstruction algorithm works slightly better with the CLIC momentum distribution than with the Gaussian momentum distribution. The reason is that more eigenvalues of the CLIC contamination matrix are relatively large while for a Gaussian many eigenvalues are very small.

When the noise level increases, the cut-off value on the eigenvalues must also increase. On the other hand, the eigenvalues are needed to lift the smearing caused by the momentum spread. When the added noise reaches roughly 8% of the maximum intensity the reconstruction fails. Beyond this level it becomes impossible to reach the balance between efficient noise reduction and getting a faithful reconstruction of the initial distribution.

The achievable spatial and temporal resolution of the horizontal beam size is determined by the vertical beam size, which adds smearing in the vertical direction, the pixel noise of the picture and the pixel size. The latter can be made negligible by a suitable imaging system and we do not consider it further.

The influence of the vertical beam size can be accounted for by convoluting the image on the screen with a Gaussian filter that represents the vertical beam size. This changes the smearing matrix F in Eq. (23) to $F' = VF$, where V is band diagonal with the Gaussian filter coefficients repeated on each row. We consider a beam having the vertical beam size half that of the horizontal beam size. This implies also that the vertical beam size is moderate compared to the vertical dispersive smearing, whose scale is given by $L\varphi_0$. By inverting F' instead of F we can recover the initial horizontal beam size, provided the noise level on the pixels is somewhat smaller than the one we had for inverting F alone. The matrix V changes the eigenvalue spectrum of F' and causes an ambiguity to find the cutoff value λ_{cut} in the matrix inversion. This analysis indicates that our method still works for beams with vertical beam size moderately smaller than the maximum dispersive smearing. The details, however, depend on the momentum distribution and the ensuant eigenvalue spectrum.

In order to address the effect of the pixel noise we calculate the amplification factor of the pixel noise of the image R on the noise level of the reconstructed distribution G which is given by the diagonal elements of the covariance matrix $(F^TF)^{-1}$. Reconstructing the horizontal width, however, is only affected weakly, despite large amplification factors between 10 and 20 for the CLIC distribution and even larger if the effect of the vertical beam size is included. This analysis indicates that the horizontal width can be determined, provided the noise level in the reconstructed image stays below 50% of the maximum values the pixels can assume.

Here, we have described a method to analyze the beam size measurement based on a linear sweep. The measurement procedure to extract time-resolved information on the momentum distribution and the geometric distribution has thus been fully described. We will now address the two most important technical aspects of the measurement system.

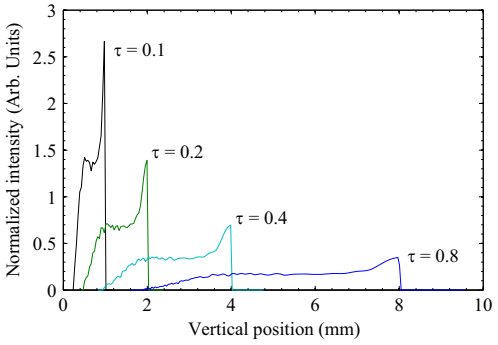

Fig. 13. The CLIC momentum distribution in the vertical plane for selected points in time. Every profile corresponds to a bunch with a given arrival time τ. The large spread leads to contamination from the late bunches of the regions where the early bunches are imaged.

5. The magnets

In Section 3 we stated in Eq. (7) the relationship between the particle coordinates on the screen to the momentum and arrival time of the particle. Two kicker systems are required for extracting the information: one for deflecting the beam in the horizontal direction (x), the other for deflecting the beam in the vertical direction (y). Each should ideally produce a sinusoidal field, with the period of the oscillation slightly longer than the 240 ns bunch train duration. The two kicker magnets would be powered 90° out of phase, equivalent to having a sine variation in y and cosine in x. The exact oscillation period will most likely be designed to be non-adjustable and in the range of 250–300 ns. The bunch trains arrive each 20 ms, hence there can be field in the kicker magnets just prior to the arrival of a bunch train, and similarly just after the

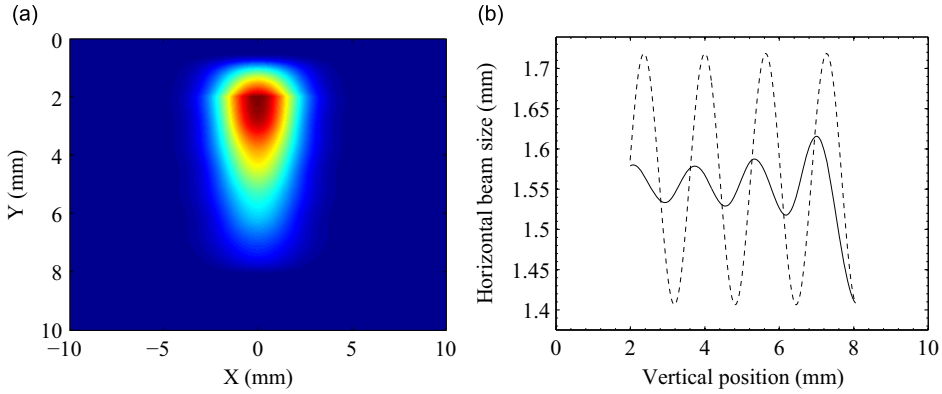

Fig. 14. When imaged on the screen (a) using a linear sweep the momentum distribution corresponding to the decelerated CLIC drive beam distorts the geometric distribution and the beam size variation in time is completely hidden through momentum smearing. The horizontal beam size calculated for each and every vertical slice is shown as a solid line in (b). Again, we display the monochromatic equivalent beam size as a dashed line. The original distribution can be recovered by solving the matrix equation in Eq. (23).

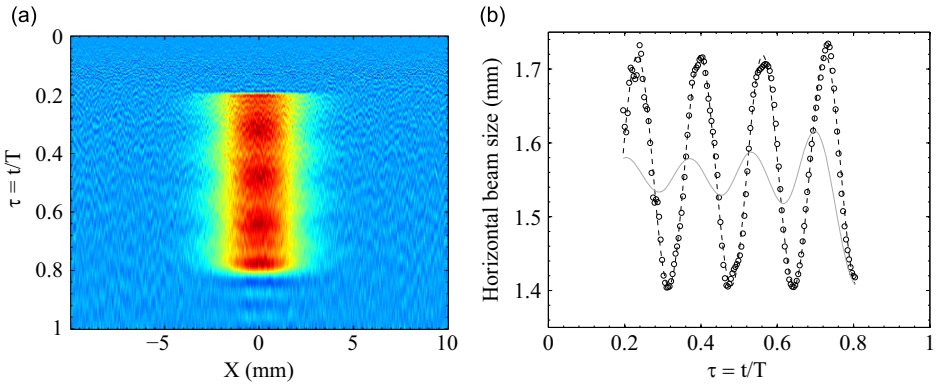

Fig. 15. Uniform noise of 1% of the maximum intensity has been added to the original image in Fig. 14(a). Then, through the matrix formulation in Eq. (23), the geometric distribution (a) can be recovered. The extracted rms horizontal beam width along the pulse (b) agrees with the original input. The beam size extracted before deconvolution is shown for comparison.

bunch train has passed through. Therefore, the conceptual design of the kicker system is to have two power supplies, one associated with each kicker magnet. When the output of the power supplies is turned on each will form a resonant circuit with the inductance of the associated kicker magnet to produce a quasi-sinusoidal waveform. The output of the power supply for the horizontally deflecting kicker magnet will be turned on such that the field is at a peak of the sinusoid when the bunch train arrives, as illustrated with the dashed line in Fig. 16, whereas the field in the vertically deflecting kicker magnet will start to rise near to the arrival of the bunch train.

Each kicker system for deflecting the decelerated CLIC drive beam, by up to 10 mrad, must provide a total kick of approximately $8.2 \cdot 10^{-3}$ Tm. In order to achieve a quasi-sinusoidal field with a relatively short period, in the range of 250–300 ns, it is presently envisaged that the kicker magnets would be of a lumped inductance design, and have a single turn to give a relatively low inductance. In order to achieve high reliability of the power supply, and a repetition rate of 50 Hz, the switch on the output stage of each power supply would most likely use power semiconductors. The proximity of the power supplies to the kicker magnets will be determined by several factors including radiation levels. In the present, conceptual, design it is assumed that each power supply will be connected to its kicker magnet by a cable of length 3 m. In order to minimize inductance, and limit radiated electromagnetic noise, each power supply and magnet would be interconnected with suitable coaxial cable. In addition the cable would be terminated in its characteristic impedance Z at the magnet end, see Fig. 17, to minimize reflections and distortion of the sinusoidal field.

A preliminary, conceptual design assumes that the aperture of both kicker magnets is 25 mm × 25 mm, and each kicker has an effective magnetic length of 0.5 m. A suitable material for the yoke is a NiZn ferrite such as 8C11 (Ferroxcube) or CMD5005 (Ceramic Magnetics). The 25 mm × 25 mm aperture does not allow any space for a ceramic tube or beam coupling impedance reduction techniques. If these are necessary the size of the aperture would be increased requiring higher current, for a given magnetic length, and thus higher supply voltage, to achieve the required integrated field. The above assumptions result in an inductance of 0.63 μH for each kicker magnet. Fig. 17 shows a simplified schematic of one power supply and its kicker magnet. The choice of cable impedance, to interconnect a power supply and kicker magnet, is a compromise between a high impedance in order to minimize damping of the sinusoidal field (especially for the horizontal deflection, which will start a quarter-period before the vertical deflection), and a low value to minimize the period of the sinusoidal oscillation: minimizing the cable impedance allows

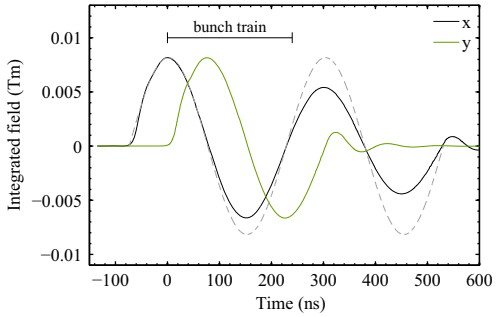

Fig. 16. Preliminary predictions for the integrated field for the x-deflecting and y-deflecting kicker magnets, as a function of time, for the conceptual design of kicker and power supply. A sine function is displayed with a dashed line for comparison with the calculated values.

the storage value capacitor to be increased and the voltage to be reduced – this is an advantage for the semiconductor switches. In addition it is advantageous to use commercially available coaxial cable; assuming a 50 Ω characteristic impedance, and neglecting parasitic capacitance, inductance and resistance, the storage capacitor value would be approximately 1.5 nF. Hence, the storage-capacitor would need to be pre-charged to approximately 11.2 kV in order to provide the required peak integrated field; the switch current would be approximately 300 A peak.

The semiconductor switches would most likely be a series and parallel array of high voltage (1 kV) MOSFETs, together with anti-parallel diodes for conducting the current associated with the negative field. The configuration would need to be carefully chosen to switch-on fast and have reasonably low on-state resistance. Fig. 16 shows preliminary predictions for the integrated field for the x-deflecting and y-deflecting kicker magnets, as a function of time, for the conceptual design of kicker and power supply. As a result of circuit losses the sinusoidal field is damped, and the first negative peak is approximately 80% of the magnitude of the first positive peak of field. Although a perfect sinusoidal field shape is the ideal, it is still possible to perform the suggested measurement with this field. Exponential damping can be incorporated in the algorithm in a straightforward way, thus accounting for the discrepancy so that the momentum distribution can be computed.

Further, detailed, design work would be required to optimize the design of kicker magnet and power supply, including careful choice of all the components. However this would also require careful adaptation to the situation in the tunnel and an evaluation of radiation in order to properly choose the length of coaxial cable between a power supply and its kicker magnet. For example, reducing the length of coaxial cable required to interconnect a

power supply and magnet from 3 m to 1 m would allow the kicker magnet length to be increased (requiring less current to achieve the same deflection), the storage capacitor value to be increased or a combination of the two: this would also result in the storage capacitor voltage being significantly decreased.

One way of generating a magnetic field suitable for the linear sweep needed for the time-resolved beam size measurement is to use the linear part of a sine wave. It is then enough to increase the oscillation period of the magnetic field while slightly increasing the field strength. This, however, would require a second power supply section, similar to the one presented in Fig. 17 but with a storage capacitor approximately 100 times the value of the storage capacitor in the first section. The power supply voltage of the second section would be up to say 20% of the value of the first section, i.e. around 2.4 kV, in order to provide up to twice the current of the first section. Finally, the antiparallel diode in Fig. 17 could be replaced with a fast switch with an antiparallel diode for switching between the circular and the linear sweep.

6. The OTR screen

The CLIC drive beam carries high power in a relatively small cross-section, thus constituting a threat to any invasive beam monitor. The post-PETS diagnostic line, however, has the advantage of diluting the beam over a large surface. Nonetheless, a study of the reaction of the screen to the beam is needed. We have considered three screen materials: aluminum, beryllium, and silicon carbide (SiC); all commonly used for ultra-high vacuum windows or screens. At the energy levels in question the stopping power of these materials is dominated by radiative effects, and the differential energy loss in beryllium is roughly a factor two lower than in aluminum and SiC. In total, the thermal–mechanical behavior of the screen depends also on thermal conductivity and expansion, specific heat capacity, elastic modulus and tensile strength of the material. The values of these properties for the three materials are listed in Table 1.

For an accurate estimate of the energy deposition in the screen we performed Monte Carlo simulations with the FLUKA code [33,34]. For symmetry reasons we use only one quarter of the

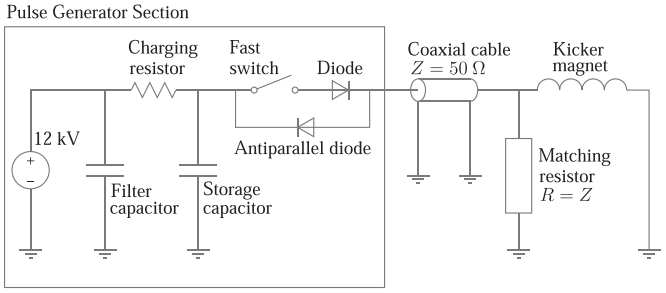

Fig. 17. Simplified schematic of one power supply and its kicker magnet.

Table 1
Thermal and mechanical properties of potential screen materials at room temperature [28–32].

Property	Symbol	Unit	Al	Be	SiC
Density	ρ	g/cm ^{3}	2.70	1.85	3.16
Specific heat capacity	C_p	J/g K	0.903	1.83	0.75
Thermal conductivity	λ	W/K m	238	230	120
Thermal expansion	α	μm/K m	23.2	11.5	4.0
Young's modulus	E	GPa	69	300	410
Tensile strength	σ_t	MPa	13	344	–

Table 2
Selected beam parameters of the CLIC decelerator [35], used for the estimation of temperature rise in the screen.

Property	Unit	Value
Bunch train repetition rate	Hz	50
Bunch train duration	ns	240
Bunch charge	nC	8.4
Bunches per train	#	2922
Bunch spacing	ps	83

screen, consisting of a 0.1 mm thin foil in vacuum. The beam is given negligible intrinsic size, so that the beam size on the screen is only due to the momentum spread and the rotating magnetic field. The momentum distribution is taken from Fig. 1(b) and the dispersion for the peak momentum is 2.5 cm. The beam parameters used for these calculations are given in Table 2.

Fig. 18(a) shows the transverse distribution of the energy deposition in the beryllium foil. The result has been scaled so as to represent the energy deposition from one bunch train, 240 ns long. Because of its short duration, the bunch train passage can be considered instantaneous, from a cooling point of view, i.e. heat dissipation occurs only in between trains and is negligible within the train. The maximum energy density of 7 J/cm^3 (or 0.07 J/cm^2 when taking the foil thickness into account) causes a local increase in temperature of $\Delta T = 1.8$ K. The equivalent numbers for the aluminum and SiC foils are 12 J/cm^3 and 10 J/cm^3 energy density, and 4.2 K and 4.5 K temperature rise, respectively. We studied the thermal response of the screen to repetitive bunch train crossings, under the assumption that the rim of the screen is kept at 300 K. Using material properties as in Table 1, we looked at the effect of conduction as well as radiation cooling of the screen in between bunch trains. While the latter is very small the conduction may be enough to keep the screen below its melting point, though this depends strongly on, e.g. the thermal conductivity. This value, however, varies with, e.g., production method when it comes to composite materials like SiC, which is why a careful study is needed for the final design. Nonetheless, we conclude that the rather modest heat increase allows for operating the diagnostic, if not at the full 50 Hz pulse repetition rate, at least at reduced rate.

In addition to the instantaneous temperature increase we investigate the cyclic thermal stress induced by many bunch train crossings. Using the maximum instantaneous temperature increase ΔT, together with the thermal expansion coefficient α and Young's modulus E from Table 1 we estimate the cyclic thermal stress to be $\sigma_c = (1/2)\Delta T \alpha E$ [36], resulting in 3–5 MPa for the materials in question. This must be compared to the tensile strength σ_t of the material, which in the case of beryllium is more than one order of magnitude larger than the induced stress. Aluminum in its pure form, however, has a yield strength of the order of 10 MPa, comparable to the cyclic stress. The tensile strength of SiC varies greatly depending on production method, which means it is difficult to make general judgement on its suitability. We conclude that a beryllium screen would be suitable for the post-PETS diagnostic line, though it is a material that must be handled with extreme care due to its toxic nature.

It is clear that the screen cannot sustain the beam in focused mode, i.e. the screen must be protected against failure scenarios, in particular the failure of the magnets. To this end, the screen geometry will be as sketched in Fig. 18(b): The screen may be either circular or rectangular, and large enough to fit a circle of radius $R \gtrsim L\varphi_0/(1+\delta_{min})$ in order to collect the most decelerated particle of momentum deviation $\delta_{min} \approx 0$. At the center we foresee a circular opening of radius $r \lesssim L\varphi_0/(1+\delta_{max})$ so that when the magnets are turned off the beam can pass the screen without crossing its surface. When the magnets are on, the least

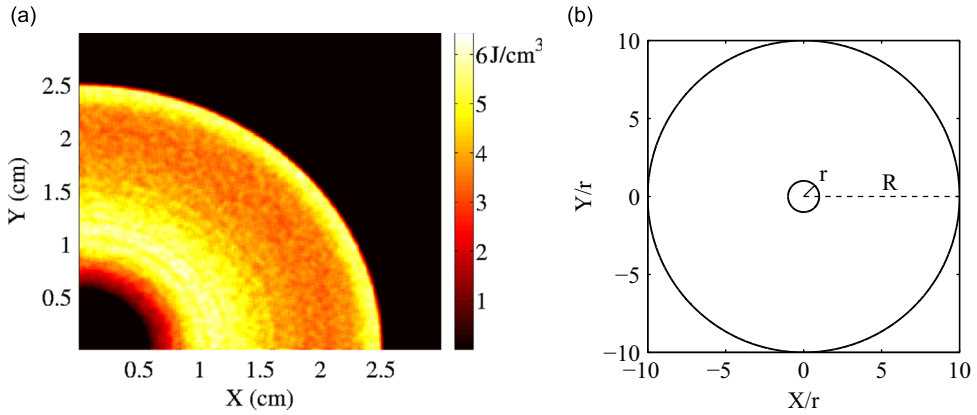

Fig. 18. The OTR screen: (a) FLUKA simulation of the energy deposited in the screen at one bunch train crossing. The screen consists of a 0.1 mm beryllium foil (b) with an outer radius $R \gtrsim L\varphi_0/(1+\delta_{min}) = L\varphi_0$ and inner radius $r \lesssim L\varphi_0/(1+\delta_{max}) = R/10$. The purpose of the hollow center is to let the non-deflected beam through without crossing the screen foil.

decelerated particle with $\delta_{max} = 9$ shall hit the screen. Note that although this screen design is intended for avoiding the high beam intensity in a small spot size it also allows us to operate the diagnostic line at a reduced bunch train repetition rate. Thus it offers extra precaution in terms of the high beam intensity.

7. Conclusions

We found that beams with large momentum spread lead to distorted images on a screen in a spectrometer if interpreted within a linearized model of the dispersion. We then derived the map that permits us to extract the correct momentum distribution from the screen image.

Using that information we propose a method to derive the time-resolved momentum distribution along the drive beam pulse from a single-shot screen image created by sweeping the beam in a circular pattern. It turned out that the momentum distribution can be recovered accurately as long as the geometric beam size is smaller than the beam size due to the finite momentum spread. For the CLIC decelerator in particular, we expect the method to become a convenient tuning tool, because the deceleration and thereby the power production can be optimized by making the circle as big as possible and the initial transient as short as possible.

The beam size variation along the pulse can be extracted by applying a linear sweep in one direction, here vertical, and recording the beam width in the horizontal plane. We showed how to disentangle the complex smearing of the transverse profile in the horizontal plane into the sweeping plane, when the momentum distribution is known. In addition, we expect that large variations of the transverse beam sizes along the pulse are visible directly and permit tuning of the decelerator and preceding beam lines. By first performing the circular sweep and then the linear sweep, the momentum distribution and beam size along the bunch train can be determined in only two shots.

In this report we finally address practical issues of the diagnostic section. A preliminary study of the thermal–mechanical stability of the OTR screen indicates that a beryllium foil can be used. In addition, a conceptual design of the kicker magnets was presented. It is probably advisable to install additional kicker magnets to create a closed bump in order to steer the deflected beams, with the large beam power, to the dump in a controlled way.

The methodology for diagnosing beams with large momentum spread was specifically developed for the CLIC drive beam. However, we expect that it will be useful in other circumstances where extreme momentum distributions can occur. The CLIC post-collision line was already mentioned in this context.

Acknowledgments

We gratefully acknowledge E. Adli, Oslo University, for providing the momentum distribution at the end of the CLIC drive beam decelerator. We thank also H. Day at CERN for valuable input on the magnet kicker design, and Natasa Slodje and Joakim Lindblad, Uppsala University, for their generous advice on image processing techniques.

References

[1] A Multi-TeV Linear Collider Based on CLIC Technology: CLIC Conceptual Design Report, CERN-2012-007, 2012.
[2] W. Panofsky, A Mass Sensitive Deflector for High-Energy Particles, HEPL-82, 1956.
[3] P.R. Phillips, Review of Scientific Instruments 32 (1) (1961) 13. http://dx.doi.org/10.1063/1.1717133.
[4] J. Haimson, IEEE Transactions on Nuclear Science NS-12 (1965) 996 (PAC65).
[5] J. Haimson, B. Mecklenburg, G. Stowell, B. Ishii, AIP Conference Proceedings 647 (1) (2002) 810. http://dx.doi.org/10.1063/1.1524936, URL http://scitation.aip.org/content/aip/proceeding/aipcp/10.1063/1.1524936.
[6] J. Haimson, AIP Conference Proceedings 737 (1) (2004) 95. http://dx.doi.org/10.1063/1.1842537. URL http://scitation.aip.org/content/aip/proceeding/aipcp/10.1063/1.1842537.
[7] D.X. Wang, G.A. Krafft, C.K. Sinclair, Physical Review E 57 (1998) 2283. http://dx.doi.org/10.1103/PhysRevE.57.2283, URL http://link.aps.org/doi/10.1103/PhysRevE.57.2283.
[8] M. Röhrs, C. Gerth, H. Schlarb, B. Schmidt, P. Schmuser, Physical Review Special Topics – Accelerators and Beams 12 (2009) 050704. http://dx.doi.org/10.1103/PhysRevSTAB.12.050704.
[9] D. Alesini, G. di Pirro, L. Ficcadenti, A. Mostacci, L. Palumbo, J. Rosenzweig, C. Vaccarezza, Detectors and Associated Equipment 568 (2) (2006) 488. http://dx.doi.org/10.1016/j.nima.2006.07.050, URL ⟨http://www.sciencedirect.com/science/article/pii/S0168900206013040⟩.
[10] P. Craievich, S. Di Mitri, M. Ferianis, M. Veronese, M. Petronio, D. Alesini, A transverse rf deflecting cavity for the FERMI@ELETTRA project, in: Proceedings of DIPAC 2007, Venice, Italy, 2007, pp. 168–170.
[11] R.J. England, J.B. Rosenzweig, G. Travish, Physical Review Letters 100 (2008) 214802. http://dx.doi.org/10.1103/PhysRevLett.100.214802, URL http://link.aps.org/doi/10.1103/PhysRevLett.100.214802.
[12] A. Mostacci, M. Bellaveglia, E. Chiadroni, A. Cianchi, M. Ferrario, D. Filippetto, G. Gatti, C. Ronsivalle, Physical Review Special Topics – Accelerators and Beams 15 (2012) 082802. http://dx.doi.org/10.1103/PhysRevSTAB.15.082802.
[13] M. Olvegård, V. Ziemann, Detectors and Associated Equipment 707 (0) (2013) 114. http://dx.doi.org/10.1016/j.nima.2012.12.114, URL ⟨http://www.sciencedirect.com/science/article/pii/S0168900212016762⟩.
[14] M. Olvegård, Emittance and Energy Diagnostics for Electron Beams with Large Momentum Spread (Ph.D. thesis), University of Uppsala, Uppsala, Sweden, 2013.

[15] A. Ferrari, V. Ziemann, R.B. Appleby, M.D. Salt, Physical Review Special Topics – Accelerators and Beams 12 (2009) 021001. http://dx.doi.org/10.1103/PhysRevSTAB.12.021001.
[16] E. Adli, A Study of the Beam Physics in the CLIC Drive Beam Decelerator (Ph.D. thesis), University of Oslo, Oslo, Norway, 2009.
[17] M. Olvegård, V. Ziemann, Emittance and momentum diagnostics for beams with large momentum spread, in: Proceedings of IBIC 2013, Oxford, UK, 2013, pp. 37–40.
[18] D. Schulte, PLACET: a program to simulate drive beams, in: Proceedings of EPAC 2000, Vienna, Austria, cERN-PS-2000-028 AE, 2000, pp. 1402–1404.
[19] G. Loew (Ed.), International Linear Collider Technical Review Committee. Second Report 2003, Technical Report, SLAC, SLAC-R-606, 2003.
[20] G. Geschonke, A. Ghigo, CTF3 Design Report, CERN PS-2002-008-RF; CTF-3-NOTE-2002-047; LNF-2002- 008-IR, May 2002.
[21] R.L. Lillestøl, S. Döbert, E. Adli, M. Olvegård, Physical Review Special Topics – Accelerators and Beams 17 (2014) 031003. http://dx.doi.org/10.1103/PhysRevSTAB.17.031003.
[22] M. Olvegård, E. Adli, H. Braun, E. Bravin, N. Chritin, R. Corsini, A. Dabrowski, S. Döbert, C. Dutriat, D. Egger, T. Lefèvre, O. Mete, P. Skowronski, F. Tecker, Detectors and Associated Equipment 683 (0) (2012) 29. http://dx.doi.org/10.1016/j.nima.2012.04.065, URL ⟨http://www.sciencedirect.com/science/article/pii/S0168900212004445⟩.
[23] M. Olvegård, E. Adli, W. Andreazza, B. Bolzon, E. Bravin, N. Chritin, A. Dabrowski, S. Döbert, M. Duraffourg, T. Lefèvre, R. Lillestøl, V. Ziemann, Physical Review Special Topics – Accelerators and Beams 16 (2013) 082802. http://dx.doi.org/10.1103/PhysRevSTAB.16.082802.
[24] B. Goddard, R. Riffaud, M. Sans-Merce, W. Weterings, Conceptual design of the LHC beam dumping protection elements TCDS and TCDQ, in: Proceedings of EPAC 2004, Lucerne, Switzerland, LHC-Project-Report-756; CERN-LHC-Project-Report-756, 2004, pp. 629–631.
[25] T. Lefèvre, C. Bal, E. Bravin, S. Burger, B. Goddard, S. Hutchins, T. Renaglia, A large scintillating screen for the LHC dump line, in: Proceedings of DIPAC 2007, Venice, Italy, CERN-AB-2007-023, 2007, pp. 132–134.
[26] M. Bern, D. Eppstein, Mesh generation and optimal triangulation, in: D.-Z. Du, F.K. Hwang (Eds.), Computing in Euclidean Geometry, Lecture Notes Series on Computing, vol. 1, World Scientific, Palo Alto, California, U.S.A., 1992, pp. 23–90.
[27] W. Press, B. Flannery, S. Teukolsky, W. Vetterling, Numerical Recipes, Cambridge University Press, Cambridge, U.K., 1987.
[28] C. Nordling, J. Österman, Physics Handbook for Science and Engineering, 7th ed., Studentlitteratur, Lund, Sweden, 1980, 2004.
[29] J. Moore, S. Greer, C. Davis, M. Coplan, Building Scientific Apparatus, 2nd ed., Addison-Wesley, Redwood City, California, U.S.A, 1989.
[30] D.F. Lupton, Advanced Materials and Technologies 2AI (2003) 667. http://dx.doi.org/10.1007/10689123_36.
[31] V. Vlachoudis, Flair: a powerful but user friendly graphical interface for FLUKA, in: Proceedings of the International Conference on Mathematics, Computational Methods & Reactor Physics (M&C 2009), Saratoga Springs, New York, U.S.A., 2009.
[32] A.C. Corporation, Silicon Carbide Material Properties, Material Data Sheet ⟨http://www.accuratus.com/pdf/sicprops.pdf⟩ (accessed 15.04.15, 15:45).
[33] A. Ferrari, P.R. Sala, A. Fasso, J. Ranft, FLUKA: A Multi-Particle Transport Code (Program Version 2005), CERN-2005-10; INFN/TC_05/11; SLAC-R-773, CERN, Geneva, 2005.
[34] G. Battistoni, F. Cerutti, A. Fasso, A. Ferrari, S. Muraroi, J. Ranft, S. Roesler, P.R. Sala, AIP Conference Proceedings 896 (2007) 31 (19 p, SLAC-REPRINT-2007-184).
[35] H.H. Braun, et al., CLIC 2008 Parameters, CLIC-Note-764, October 2008.
[36] M. Seidel, An Exit Window for the TESLA Test Facility, TESLA Report 1995-18, DESY, August 1995.